

Accepted to ApJ, May 10, 2022

GAS BULK MOTION IN THE PERSEUS CLUSTER MEASURED WITH *Suzaku*

T. Tamura, N. Yamasaki, R. Iizuka

*Institute of Space and Astronautical Science, Japan Aerospace Exploration Agency,
3-1-1 Yoshinodai, Chuo-ku, Sagami-hara, Kanagawa 229-8510, Japan*

Y. Fukazawa

*Department of Physical Science, Hiroshima University, 1-3-1 Kagamiyama,
Higashi-Hiroshima, Hiroshima 739-8526, Japan*

K. Hayashida, S. Ueda

*Department of Earth and Space Science, Graduate School of Science, Osaka University,
Toyonaka 560-0043, Osaka, Japan*

K. Matsushita, K. Sato

*Department of Physics, Tokyo University of Science, 1-3 Kagurazaka, Shinjyuku-ku, Tokyo
162-8601, Japan*

K. Nakazawa

*Department of Physics, The University of Tokyo, 7-3-1 Hongo, Bunkyo-ku, Tokyo
113-0033, Japan*

N. Ota

*Department of Physics, Nara Women's University, Kita-uoyanishimachi, Nara, 630-8506,
Japan*

M. Takizawa

*Department of Physics, Yamagata University, 1-4-12 Kojirakawa-machi, Yamagata,
990-8560, Japan*

ABSTRACT

We present the results from *Suzaku* observations of the Perseus galaxy cluster, which is relatively close, the brightest in the X-ray sky and a relaxed object with a cool core. A number of exposures of central regions and offset pointing with the X-ray Imaging Spectrometer cover a region within radii of $20' - 30'$. The central data are used to evaluate the instrumental energy-scale calibration with accuracy confirmed to within around 300 km s^{-1} by the spatial and temporal variation of the instruments. These deep and well-calibrated data are used to measure X-ray redshifts of the intracluster medium. A hint of gas bulk motion, with radial velocity of about $-(150 - 300) \text{ km s}^{-1}$ relative to the main system was found at $2 - 4$ arcmin ($45 - 90 \text{ kpc}$) west of the cluster center, where an X-ray excess and a cold front were found previously. No other velocity structure was discovered. Over spatial scales of $50 - 100 \text{ kpc}$ and within 200 kpc radii of the center, the gas-radial-velocity variation is below 300 km s^{-1} , while over scales of 400 kpc within 600 kpc radii, the variation is below 600 km s^{-1} . These X-ray redshift distributions are compared spatially with those of optical member galaxies for the first time in galaxy clusters. Based on X-ray line widths gas turbulent velocities within these regions are also constrained within $1000 - 3000 \text{ km s}^{-1}$. These results of gas dynamics in the core and larger scales in association with cluster merger activities are discussed and future potential of high-energy resolution spectroscopy with ASTRO-H is considered.

Subject headings: galaxies: clusters: general — galaxies: clusters: individual (Perseus) — X-rays: galaxies: clusters

1. INTRODUCTION

Galaxy clusters are the largest and youngest gravitationally-bound cosmic structure and form hierarchically through collisions and mergers of smaller systems. Spatial and radial velocity distributions of member galaxies and X-ray observations of the intracluster medium (ICM) have revealed that some systems are still forming and unrelaxed. Along with gravitational lensing observations, these studies have provided dynamical measurements of dark matter in clusters.

As the structure forms, gravitational potential governed by dark matter pulls and thus heats the ICM through shocks. Sharp X-ray images obtained by *Chandra* revealed shocks and density discontinuities (so-called “cold fronts”) suggesting supersonic or transonic gas motions, respectively (see Markevitch & Vikhlinin 2007, for a review). These heating processes would then develop gas turbulence, and accelerate particles, which in turn generate diffuse

radio halos and relics. The activities of central massive black holes also disturb and warm up the gas around cluster cores. The motion of gas should be measured to facilitate direct understanding of these energy flows. Constraining total energy distribution in a system allows the total gravitational mass to be measured, as required for precise cosmology. Energies in gas random or ordered motions could be the key uncertainty to calibrate total mass distribution, as suggested by numerical simulations (e.g. Evrard et al. 1996; Nagai et al. 2007; Takizawa et al. 2010; Suto et al. 2013).

Gas bulk or turbulent motions can be measured directly using the Doppler shift or by broadening of X-ray line emissions. However, the limited energy resolutions of current X-ray instruments continues to hinder such measurements. For example typical CCD energy resolution is about 130 eV (in full width half maximum; FWHM), compared with a possible energy shift of ~ 20 eV corresponding to a radial velocity of 1000 km s^{-1} , all at the Fe-K line energy.

The *Suzaku* XIS (Koyama et al. 2007) is currently the optimal X-ray spectrometer for gas motion search with Fe-K lines, as was demonstrated when gas bulk motion was detected in a merging cluster, Abell 2256, by Tamura et al. (2011). In addition, XIS data imposed tight constraints on gas motion in a number of clusters, as summarized in Table 1.

Numerical studies have striven to clarify cluster formation histories and the associated origins, development, and dissipation of various types of gas motions. However, by nature cluster evolution is governed by random processes, which means systematic measurements of systems in a wide range of evolution stages are also required as well as these theoretical efforts. The geometrically-complex nature of gas dynamics should be spatially resolved. For example, gas dynamics in apparently relaxed clusters should be studied as demonstrated by (Ota et al. 2007, hereafter OTA07) using early *Suzaku* observations of the Centaurus cluster. To improve the limit of gas bulk motion in a relaxed system, we analyzed a large set of *Suzaku* data of the Perseus cluster.

The Perseus cluster, the brightest in X-ray, is a prototype of a nearby and relaxed object. At the same time, it exhibits a number of past and current activities at core and larger scales, while at the cluster center, the very peculiar central galaxy NGC 1275 displays a complex network of emission-line nebulosity. Based on the thread-like structure of filaments resolved by the Hubble Space Telescope, Fabian et al. (2008) suggested the magnetic support of the structure and ordered gas motions not highly turbulent over scales of < 10 kpc around the galaxy. The cluster X-ray emission peaks sharply toward the galaxy and its central active galactic nucleus (AGN), 3C 84. The AGN also develops jets and radio lobes where high-energy particles and X-ray-emitting-hot gas interact, as discovered by Böhringer et al. (1993). Associated with these current and possibly past AGN activities, fine gas structures

Table 1. Suzaku results of gas bulk motions in clusters.

target	result	Reference
Centaurus	$\Delta v < 1400 \text{ km s}^{-1}$	1
Oph.	$\Delta v < 3000 \text{ km s}^{-1}$	2
AMW 7	$\Delta v < 2000 \text{ km s}^{-1}$	3
A 2319	$\Delta v < 2000 \text{ km s}^{-1}$	4
A 2256	$\Delta v = 1500 \pm 300(\text{stat.}) \pm 300(\text{sys.})\text{km s}^{-1}$	5
Coma	$\Delta v < 2000 \text{ km s}^{-1}$	6
A 3627	$\Delta v < 800 \text{ km s}^{-1}$	7

Note. — Unless stated otherwise, values are 90% limit of gas velocity variation among regions within the cluster.

References. — (1) Ota et al. (2007); Velocity variation among $2' \times 2'$ regions. (2) Fujita et al. (2008). (3) Sato et al. (2008); a hint of a velocity difference between two regions is found. (4) Sugawara et al. (2009). (5) Tamura et al. (2011); errors are 68% confidence limit. stat. and sys. mean statistical and systematic errors. (6) Sato et al. (2011). (7) Nishino et al. (2012); relative velocity of a sub component.

such as bubbles, ripples, and weak shock fronts were revealed by deep *Chandra* imaging (Fabian et al. 2011, and references therein). These processes dissipate energies into various types of gas motions. Independently, based on the lack of resonant scattering of Fe-K line emissions, Churazov et al. (2004) suggested gas motions in the core of a velocity of at least half the speed of sound.

West of NGC 1275, a chain of galaxies is distributed toward another radio galaxy IC 310, while other member galaxies and clusters virtually aligned with this chain form the Pisces-Perseus supercluster. On the other hand, the ICM X-ray emission has been traced up to at least 2 Mpc with an elongation in the east-west direction. Based on the X-ray morphology of early observations, Hirayama & Ikeuchi (1978) hypothesized that the gas and galaxies are rotating with a velocity of close to 3000 km s^{-1} . Furusho et al. (2001) found asymmetrical ICM temperature distribution and suggested a past merger in the direction parallel to the line of sight. Using *XMM-Newton* Churazov et al. (2003) further studied the asymmetric structures around the core ($R < 20'$) and revealed a hot “horseshoe” surrounding the cool core. They also assumed a minor merger along the east-west direction in the sky plane. Simionescu et al. (2012) studied the gas distribution over wider spatial scale ranges and suggested mergers and associated swirling gas motions.

The cluster center has been observed twice-yearly as a calibration target of the XIS and we used all available data. The integrated deep exposure of this unique object along with the high sensitivity of the XIS provides one of the best quality X-ray spectra from clusters. We also used some offset region ($R < 30'$) data and derived larger scale ICM emission properties.

Parts of the *Suzaku* Perseus data set were used for a number of measurements. Tamura et al. (2009) reported the first detection of Cr and Mn X-ray lines from clusters and ICM elemental abundance measurements, while Matsushita et al. (2013) and Werner et al. (2013) reported abundance measurements out to the cluster outskirts. Using offset XIS data along with the HXD data, Nishino et al. (2010) reported an upper temperature limit in the outer region. Simionescu et al. (2011, 2012) measured large-scale gas thermal distribution over the viral radius.

In the next section, we describe observations and data reduction, while in section 3 we evaluate the accuracy of the XIS energy response, which is crucial to calibrate our measurement. In sections 4 and 5 we measure gas bulk velocities within the central pointing and over a larger scale respectively, for the first time in this system, which enables one of the most accurate measurements of gas bulk motion in relaxed clusters. Finally these results are summarized and discussed in the last section.

Throughout this paper, we assume the following cosmological parameters: $H_0 = 70 \text{ km}$

$s^{-1}\text{Mpc}^{-1}$, $\Omega_m = 0.3$, and $\Omega_\Lambda = 0.7$. At the cluster redshift of 0.0183, one arcmin corresponds to 22.2 kpc. We use the 68% (1σ) confidence level for errors, unless otherwise stated.

2. OBSERVATIONS AND DATA REDUCTION

The Perseus cluster center is a calibration target and the central galaxy, NGC 1275, was always located at the CCD center. We call these observations *central* pointings. Here we use the data obtained from 2006 to 2013 taken in the normal window mode and Table 2 shows an observation log. The total exposure time is 576 ks. The XIS 2 sensor was only available until November 2006. These data were used in the instrument calibration reported by Koyama et al. (2007), Ozawa et al. (2009), and Uchiyama et al. (2009).

The off-center regions were also observed many times. We call these *offset* pointings and use the data given in Table. 3. The total exposure time is 327 ks. Fig. 1 shows the field of views of the observations.

Detailed descriptions of the *Suzaku* observatory, XIS instrument, and X-ray telescope are found in Mitsuda et al. (2007), Koyama et al. (2007), and Serlemitsos et al. (2007), respectively.

The XIS field of view is a square of $17'.8 \times 17'.8$ with 1024×1024 pixels. Accordingly, 1 pixel $\simeq 1.04$ arcsec. The energy resolution is about 50 eV at 1 keV and 130 eV at 6 keV in FWHM. Initially the XIS are operated normally in the spaced-row charge injection (SCI) off mode. Since 2006 October, the SCI on has been used in normal mode.

We started the analysis from archived cleaned event files, which were filtered with standard selection criteria, and used the latest calibration file as of 2012 November 6.

We examined light curves in the 0.3–2.0 keV band excluding the central bright region events ($R < 6'$), for stable-background periods. None of the data showed any flaring event.

The XIS energy data have an original energy channel width of 3.65 eV. We grouped these by common bin sizes of about one-third of the FWHM of the energy resolution. Around the Fe-K line, the width is 8 channels or about 30 eV. To establish the XIS energy response function, we used `xisrmfgen` software alongside `makepi` (version-20121009) to assign PI values. The energy bin size is 1 eV ($\sim 0.15 \times 10^{-3}$ of the Fe-K line energy), which means we can resolve the change of energy at less than the systematic limit of about 10^{-3} . For spectra fitting, we use XSPEC (version-12.8; Arnaud 1996) and maximum likelihood (χ^2) statistics implemented in the same. Note that the above binning gives about 15 counts per bin in the lowest-count spectrum and more than 20 counts per bin in other spectra analyzed below.

Table 2. *Suzaku* central pointings of the Perseus cluster.

Name	Date	Sequence	SCI ^a	Exp ^b (ks)	Roll ^c (degree)
CEN-0602	2006 Feb	800010010	off	43.7	260.2
CEN-0608	2006 Aug	101012010	off/on	92.0	66.0
CEN-0702	2007 Feb	101012020	on	40.0	258.7
CEN-0708	2007 Aug	102011010	on	35.1	83.4
CEN-0802	2008 Feb	102012010	on	34.9	255.2
CEN-0808	2008 Aug	103004010	on	34.1	86.8
CEN-0902	2009 Feb	103004020	on	46.3	256.1
CEN-0908	2009 Aug	104018010	on	34.2	67.0
CEN-1002	2010 Feb	104019010	on	33.6	277.3
CEN-1008	2010 Aug	105009010	on	29.6	66.6
CEN-1102	2011 Feb	105009020	on	32.9	259.7
CEN-1108 ^d	2011 Aug	106005010	on	34.1	83.8
CEN-1202	2012 Feb	106005020	on	41.1	262.0
CEN-1208	2012 Aug	107005010	on	33.2	72.6
CEN-1302	2013 Feb	107005020	on	41.2	256.3

^aSpaced-row charge injection mode on or off.

^bExposure time.

^cRoll angle of the pointing defined as north to DETY axis.

^dNo XIS-3 data is available.

Table 3. *Suzaku* offset pointings of the Perseus cluster.

Name	Date	Sequence	SCI	Exp (ks)	R ^a (arcmin)	PA ^b (degree)
A	2006 Sep	801049010	off	25	36	345
B	2006 Sep	801049020	off	27	31	260
C	2006 Sep	801049030	off	31	28	140
D	2006 Sep	801049040	off	8	33	56
E	2011 Feb	805045010	on	27	18	180
F	2011 Feb	805046010	on	18	16	0
G	2011 Feb	805047010	on	17	14	110
H	2011 Feb	805048010	on	15	17	58
E1	2009 Jul	804056010	on	7	16	90
N1	2009 Aug	804063010	on	14	15	330
S1	2010 Aug	805096010	on	8	16	200
W1	2010 Aug	805103010	on	6	16	280
SE1	2011 Aug	806099010	on	11	15	140
SW1	2011 Aug	806106010	on	12	14	225
NE1	2011 Aug	806113010	on	9	16	10
F_2	2013 Feb	807019010	on	14	16	0
S1_2	2013 Feb	807020010	on	23	16	200
H_2	2013 Feb	807021010	on	18	19	58
W1_2	2013 Feb	807022010	on	23	16	280
G_2	2013 Feb	807023010	on	14	19	110

Note. — Observation D is not used in the spectral analysis, because of the low statistics.

^aDistance between cluster and pointing centers.

^bPosition angle of the pointing center with respect to the cluster center, i.e. north, east, south, and west are 0, 90, 180, and 270 degrees, respectively.

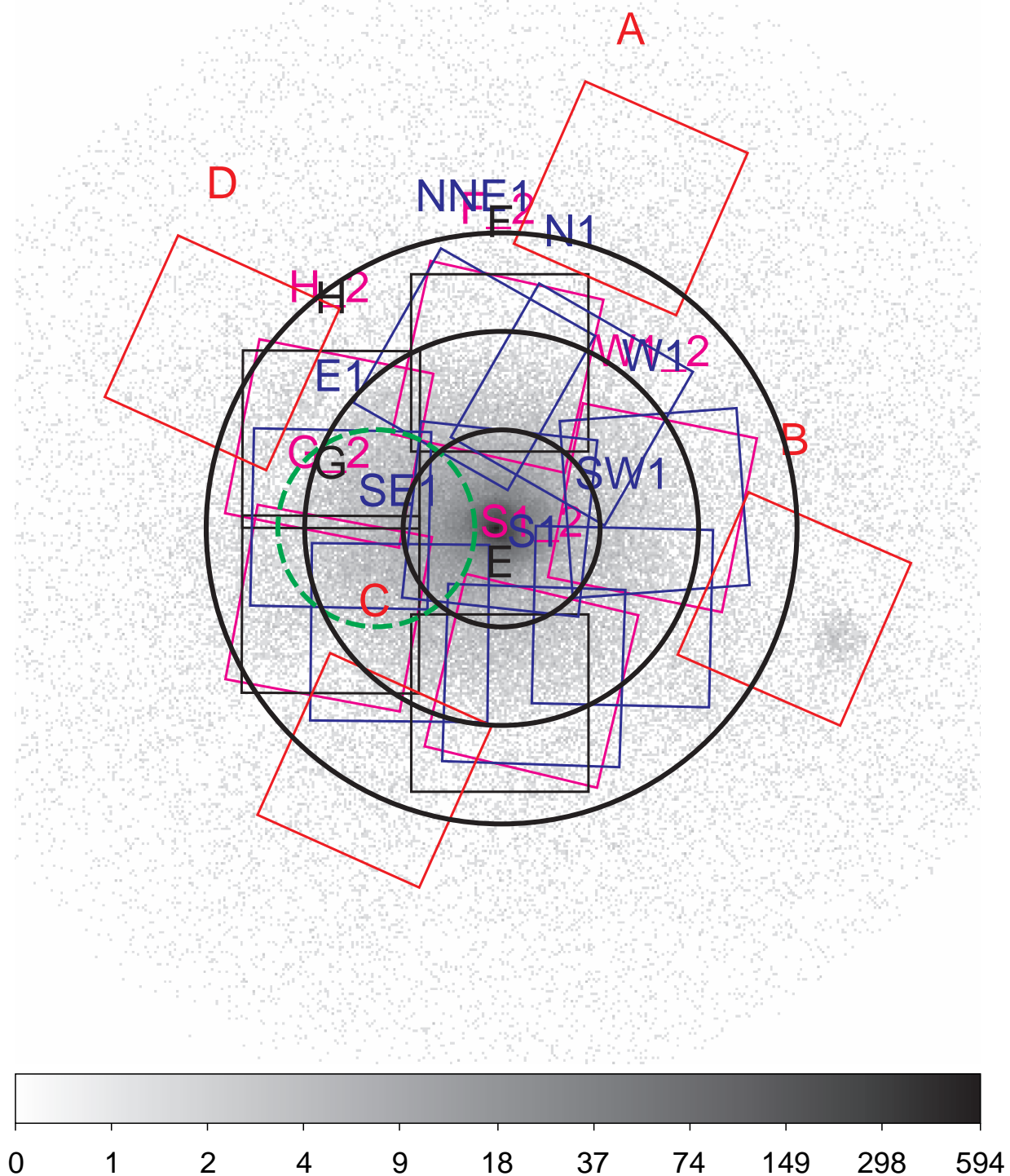


Fig. 1.— *Suzaku* observation fields on top of the ROSAT image. The XIS field of views are shown in boxes. Three circles indicate regions with radii of 10', 20' and 30'. The dashed circle indicates the east cool region found in Furusho et al. (2001). Observation-D is not used in the spectral analysis.

3. ENERGY RESPONSE CALIBRATION

3.1. Motivations

The main goal of this paper is to measure Doppler shifts of cluster K-shell iron lines in X-rays. These astronomical shifts should be separated from instrumental effects on the energy scale (i.e. recorded pulse-height vs. energy). The instrumental effects include (i) CCD-to-CCD variation, (ii) intra-chip *spatial* variations attributable to charge-transfer inefficiency (CTI) and by CCD segment-to-segment qualities, (iii) observation-to-observation *temporal* variation, (iv) absolute energy determination, and unknown systematics. These instrumental characteristics have been calibrated and extensively evaluated by the instrument team, which is an advantage of the *Suzaku* XIS over other CCD-type spectrometers. These results have also been demonstrated; not only in the cluster redshift analysis stated in section 1 but also in X-ray spectroscopy in the Galactic center and ridge (e.g. Koyama et al. 2007) and in supernova remnants (e.g. Hayato et al. 2010). We summarize the latest calibration status in subsection 3.2. Using the latest calibration and the Perseus data, we further evaluate accuracy in subsection 3.3.

Among the above instrumental variations, factor (i) can be checked by comparing observed data from different CCDs in any observations. The built-in calibration source lines are used to evaluate factors (iv) for each observation.

When analyzing the Perseus central data (section 4), factor (ii) is crucial and (iii) can be internally checked against the data. For the offset data analysis (section 5), (iii) is important. Moreover, (ii) also affects the result because each pointing observation includes different distributions of events over the detector position.

3.2. Reported Status

Koyama et al. (2007) estimated the systematic uncertainty of absolute energy in the Fe-K band to be within +0.1 and -0.05% , based on Fe lines observed from the Galactic center alongside Mn K_α and K_β lines (at 5895 and 6490 eV respectively) from the built-in calibration source (^{55}Fe). Independently, OTA07 investigated the XIS data and evaluated the energy-scale calibration in detail. Using early calibration and early Perseus cluster data (sequence 800010010), they estimated the systematic error of the *spatial* gain non-uniformity (ii) to be $\pm 0.13\%$ (68% confidence level). A similar analysis was performed by Tamura et al. (2011) using two Perseus cluster datasets with a new calibration and the accuracy was confirmed. Furthermore, Ozawa et al. (2009) systematically examined the XIS data obtained

from the start of the operation in July 2005 until December 2006 (SCI off mode data). They reported that the *spatial* dependence of the energy scale (ii) was well corrected for charge-transfer inefficiency and cited a time-averaged uncertainty of absolute energy of $\pm 0.1\%$. Uchiyama et al. (2009) reported the energy scale calibration for SCI-on mode. Sawada et al. (2012) reported an improved CTI correction. They archived energy accuracies of $< 0.7\%$ and $< 0.1\%$ at 1 keV and 7 keV, respectively, over the entire CCD position in the SCI-on mode data. We based on these calibration methods in the latest calibration files.

The energy resolution changed over time and was measured at 140 eV (July 2005; SCI off), 200 eV (April 2007 ; SCI off), and 160 eV (March 2008; SCI on) for the FI CCD at Mn $K\alpha$ in FWHM. This gradual change in energy resolution was also calibrated; the typical uncertainty of resolutions is 10–20 eV in FWHM.

3.3. Calibration Source Data

To evaluate the absolute energy scale in different CCD segments (A and D in XIS-0,1,3) we use the Perseus central pointing data (Table 2) and extracted spectra of calibration sources which illuminate two corners of each CCD. These spectra within the energy range 5.3–7.0 keV are fitted with two Gaussian lines (zero intrinsic width) for the Mn $K\alpha$ and $K\beta$ along with a bremsstrahlung continuum component. We parametrize the energy scale using a common “redshift” deviated from the expected value of 5895 eV (Mn $K\alpha$) and 6490 eV (Mn $K\beta$). Spectra from different observations, CCDs, and segments were fitted separately.

As shown in Table 4, the average redshifts are all below 10^{-3} , which indicates that the absolute energy scale is calibrated accurately if averaged over observations. The variations within each segment are comparable with statistical errors, which suggests that systematic errors in instrumental variations are below statistical ones.

Following OTA07 and based on the obtained distribution of redshifts we measure residual variation by calculating σ_{sys} such that $\chi^2 = \Sigma(z_i - \langle z \rangle)^2 / (\sigma_i^2 + \sigma_{\text{sys}}^2)$ equals the degree of freedom. Here z_i , $\langle z \rangle$, and σ_i are the obtained redshift, its average, and statistical errors, respectively. We found σ_{sys} to be 0.8×10^{-3} . This variation includes CCD-to-CCD (i), segment-to-segment (ii), and temporal (iii) factors. The calibration source is attached to the opposite side of read-out nodes of each CCD; hence the above calibration source accuracy energy indicates the precision of the CTI calibration.

Averaging the four segments of the FI-CCDs (Table 4), we obtain a redshift close to -0.1×10^{-3} , while BI redshift is close to 0.8×10^{-3} . This relatively significant BI spectral deviation, which is still within statistical errors, could introduce systematic error. Because

of better sensitivity of the FI at higher energy bands, FI is calibrated better than BI at these energy bands. Moreover the FI spectra also provide better energy resolution. In view of these properties, we use only the FI data in the following analysis.

To evaluate energy resolution calibration, we fitted the Mn lines by adding an artificial line width (σ_{add}) and found that the best-fit σ_{add} tended to be zero. The 1σ upper limit of σ_{add} ranged from 5 to 80 eV depending on the line counts with an average of 25 eV. These confirm the reported energy resolution calibration. We assume this 25 eV $\sim 1250 \text{ km s}^{-1}$ to be a 1σ systematic error in line width at around the Fe-K energy.

3.4. The Perseus Central Observations

3.4.1. Motivations

The spatial variation in the XIS energy scale [(ii) in subsection 3.1] was calibrated using Perseus cluster data as one of the primal sources. Here we use the same source but all available data (Table 2) alongside the latest calibration information and evaluate the accuracy.

We should note that the Perseus data themselves are used to correct the CTI, assuming the cluster has uniform Fe-line energy over the central region ($17'.8 \times 17'.8$). Possible deviations from this assumption could add systematic errors. We assume these systematic errors to be insignificant on the followings grounds. Firstly, the CTI parameters are determined using Perseus data observed in different roll-angles, meaning the CTI correction is not solely dependent on cluster-intrinsic distribution of Fe-line energy. Secondly, the CTI correction is not tuned for each observation, but based on instrumental characteristics as a function of the number of CCD read-out transfer (ACT-Y coordinates), CCD segments, observation time, and X-ray energy. Thirdly, built-in calibration source data along with other astronomical sources such as the Galactic center and supernova remnants (at lower energies) were used to correct and evaluate the calibration. We check the assumption more quantitatively in this subsection.

Here we group observations by their roll-angles. One group (“winter”) data were obtained in February each year with roll-angles of 255° – 277° . The other (“summer”) data were obtained in August with roll-angles of 66° – 86° . Note that pointing centers are close to each other within about 30 arcsec in all data. Within each group, different observations share roll angles close to each other, meaning a certain detector position allows a particular sky region to be observed. Using these data sets with two different extraction methods, we checked both *instrumental* and *cluster*-intrinsic variations in the energy scale.

Table 4. Variation in the measured energy scale parametrized by redshifts over observations of the Perseus central pointing. All values are in redshifts in units of 10^{-3} .

CCD/seg ^a	$\langle z \rangle^b$	s.d ^c	max-min ^d	sta.err ^e
XIS0/A	0.23	1.24	2.7	1.0
XIS0/D	0.31	1.37	2.6	0.7
XIS3/A	-0.11	0.63	1.6	1.1
XIS3/D	-0.72	1.46	4.2	1.0
XIS1/A	-0.65	1.28	3.5	0.9
XIS1/D	-0.95	1.43	2.8	1.4

^aCCD and segment.

^bAverage of redshifts.

^cStandard deviation.

^ddifference between minimum and maximum values.

^eAverage of statistical errors.

In the first extraction (subsection 3.4.2) we integrated spectra from different sky regions sorted by detector positions and found no significant variation in the line centers measured among different detector positions nor between the two-roll groups. In the second extraction, given in section 4, we integrated spectra from different detector positions sorted by sky regions. We found no significant variation among different sky regions nor between the two-roll groups. These analyses are not completely independent and we cannot completely separate *instrumental* and *cluster* variations. Nevertheless, both indicate that both *instrumental* and *cluster* variations are small and within certain error level.

3.4.2. Detector-sorted spectra

We divided the XIS field of view into 4×4 cells of size $4'.5 \times 4'.5$ in detector coordinates (DETX and DETY) as illustrated in Fig. 2. We call these cells DET00, DET01 and so on up to DET33.

Based on each cell and observation, a spectrum is extracted, whereupon each spectrum in the 5.7–7.3 keV band is fitted with two Gaussian lines for He-like $K\alpha$ (~ 6700 eV) and H-like $K\alpha$ (~ 6966 eV) and a bremsstrahlung continuum model.

As stated in subsection 4.3, since we found no need for additional line width for Gaussian lines, we fixed the width at zero henceforth. We used the common redshift of the two lines as a fitting parameter. Examples of the spectral fitting are given in Appendix (Fig. 13).

We found that the instrumental non-X-ray background is well-below the source count and subtracting the estimated background does not affect the obtained redshift, so we decided not to subtract the background from the central pointing data henceforth. We confirmed that the two FI CCD (XIS-0 and -3) spectra always give consistent line energies and this validates that CCD-to-CCD variation (i) is well calibrated, at least within the FI CCDs. We therefore combine these two CCD data henceforth. We fitted a set of spectra from individual cells (DET ij) from different observations within each roll-angle group using a common redshift. We also fitted all observations using a common redshift. The obtained redshift variations are given in Fig. 3 and Table 5.

There are two special cells, DET03 and DET33. Because these include calibration source areas, they are much smaller in area (See Fig. 2) and hence lower in counts than others. These areas are not used here and in the Perseus spectral extraction given below. In particular, the count of DET33 are lower than 10% of those in others. DET33 also shows the largest deviation from average, which could be attributable to instrumental systematic effects but also statistically. DET03 shows larger redshifts in both the two groups. In this case, the

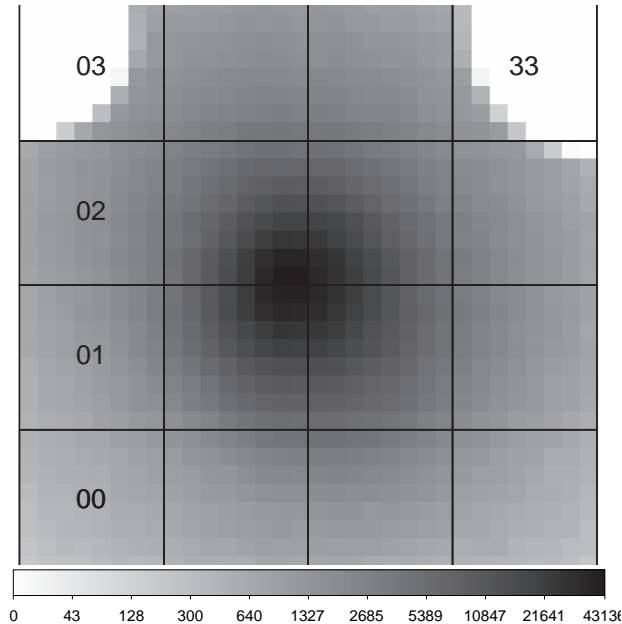


Fig. 2.— Detector cells in (DETX, DETY) coordinates overlaid on the Perseus image of XIS-0 from one observation (101012010). Parts of cell numbers are indicated. The two top corners are regions illuminated by the calibration source and excluded for spectral extraction.

deviation is more likely caused by an instrumental effect. These deviations in DET03 and DET33 are as small as $(1 - 3) \times 10^{-3}$. In addition, the sum of these two positions occupies only a small percentage of the whole CCD area, which means any systematic errors have little effect on our measurements.

We found that standard deviations, σ_{sd} , among the detector positions for each roll-group and for all observations are $(0.8 - 1.6) \times 10^{-3}$ in redshift (Table 5). If we exclude the DET33 result, these are reduced to $\sim 0.6 \times 10^{-3}$. These variations are attributable to the combination of *instrumental* and *cluster* variations.

In the DET23 cell, two-roll-group spectra reveal the largest difference, 2.0×10^{-3} , in redshifts, but elsewhere, they give consistent redshifts. Noting that different sky regions are observed by both groups in the same detector position, this indicates that *cluster*-intrinsic variation is below these differences.

Further analysis of smaller spatial scales is limited by statistics, but we assume that the instrumental energy scale does not change on such scales.

Based on these analysis, we conclude that the CCD-to-CCD variation [(i) in subsec-

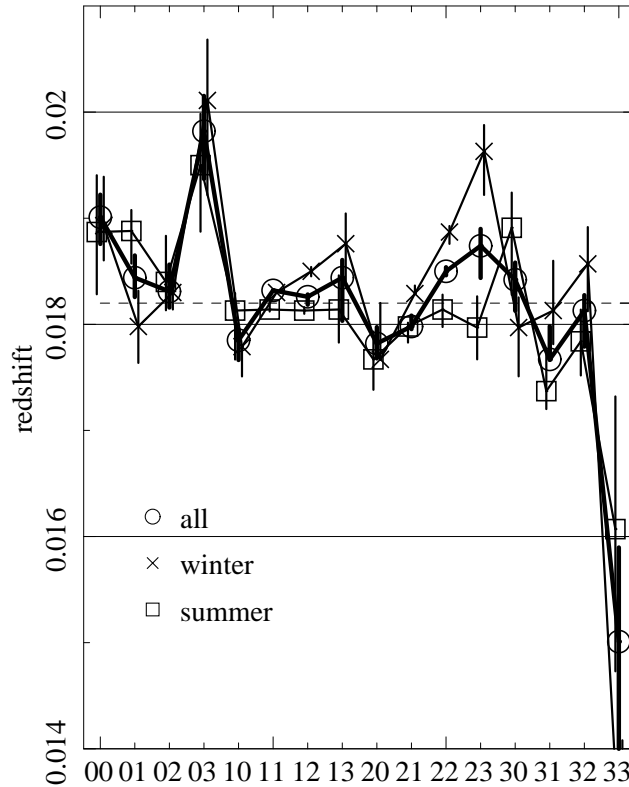


Fig. 3.— Redshift (energy-scale) variations from spectra sorted by detector positions (X-axis). Results from “winter” and “summer” roll-angles and all observations are given by different symbols.

tion 3.1] and intra-chip *spatial* variation (ii) within spatial scales of a few arcminutes is below 0.1% (10^{-3} in redshift or 300 km s^{-1} around the Fe-K energy) over the whole CCD position.

4. CENTRAL POINTING SPECTRA

Here we use a set of central pointing data of the Perseus cluster and investigate the spatial distribution of spectral properties within the central region ($\sim 17'.6 \times 17'.6$).

Table 5. Variations of measured redshifts from spectra sorted by detector positions. All values are in redshifts in units of 10^{-3} .

roll-group	$\langle z \rangle$	σ_{sd}^a	max-min ^b	sta.err ^c
All (16) positions				
winter	18.2	1.6	5.9	0.39
summer	18.1	0.78	1.7	0.33
all	18.2	1.0	3.4	0.23
Excluding DET33 (15 positions)				
winter	18.5	0.66	0.91	0.28
summer	18.2	0.59	0.41	0.25
all	18.4	0.56	0.60	0.18

^aStandard deviation.

^bDifference between minimum and maximum values.

^cAverage statistical error.

4.1. Spectral Extraction

We divided the central sky region into cells of sizes $2'.2 \times 2'.2$ or $4'.4 \times 4'.4$, as illustrated in Fig. 4. We call inner and smaller cells CS_i and larger cells CL_i , with i ranging from 0 to 15, starting from the south-west corner toward the north-east. Note that the sum of $CL_5, CL_6, CL_9,$ and CL_{10} overlap with CS_0 – CS_{15} . From each cell and each observation one spectrum is extracted.

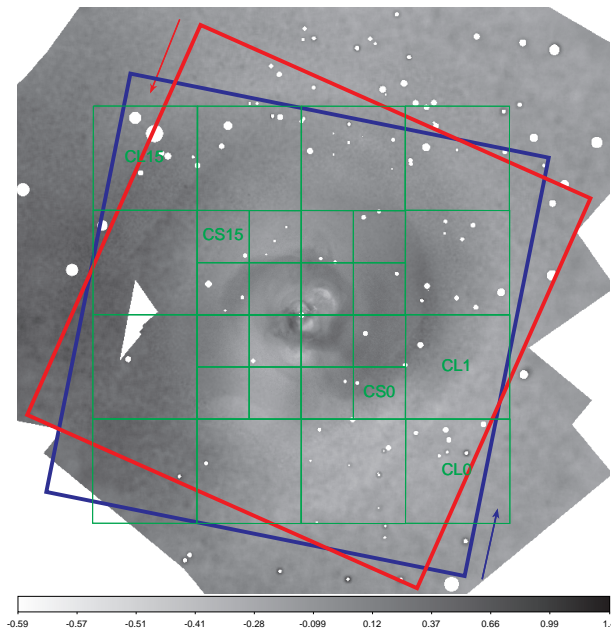


Fig. 4.— Spectral extraction cells in (RA, DEC) coordinates (in green) along with a *Chandra* image of the cluster. The *Chandra* image shows the fractional difference to the average at each radius taken from (Fabian et al. 2011, Fig.2). Some of cell names are indicated. North is up and west is right. Two squares indicate XIS field of views by a single observation in the summer roll-angle group in red and another in the winter roll-angle group in blue. Arrows indicate the DETY direction from (DETX,DETY)=(0,0) corner for each observation.

Before measuring redshifts, we evaluate spectra by fitting them in the 2.0–9.0 keV energy band with a single temperature model and the Galactic absorption (hydrogen column density of $1.5 \times 10^{-21} \text{cm}^{-2}$) and determine the temperature and metal abundance of each region. We found a two-dimensional temperature variations of 4.5–6.5 keV. Conversely, the metallicity increased radially from 0.3 to 0.45 solar toward the center. These results match previous measurements and confirm that these spectra can be used to measure local properties from different sky regions.

4.2. Redshift Measurements

We measure redshifts based on the Fe-K line center and the same model (two Gaussians and a bremsstrahlung continuum) as in section 3.4. Fig. 5 shows fitting examples. The redshift variation as a function of observation and hence observation date is shown in Fig. 6. Spectra from the first observation (sequence 800010010) show systematically smaller redshift. Other than this, however, there is no systematic change over the observation period, confirming that the *temporal* variation in the energy scale is effectively corrected.

To compensate possible observation-dependence of the energy scale, we measure the redshift relative to that of a bright cell (CS5 or CL5) for each observation and each sky cell, Δz . Fig.7 shows Δz averaged over observations. Here we measure the error ($\sigma_{\text{sd,all}}$) for each cell based on standard deviation among all observations. These observations differ in terms of the detector orientation (i.e. roll-angle) and observation-date. Therefore the scope of error includes not only statistical errors but also at least partially systematic errors due to instrumental energy-scale variations. Along with average values from all observations, those from summer and winter roll-angle observations are given separately. Differences between the two-roll-angle observations enable systematic errors from instrumental effects to be estimated. In all cases, however, the differences are below 2×10^{-3} , confirming that the *instrumental* variation is insignificant as described in section 3.4.

The largest $|\Delta z|$ is 1.5×10^{-3} at CL0, where $\sigma_{\text{sd,all}}$ is about 1.9×10^{-3} . All other regions have $|\Delta z|$ below 1.0×10^{-3} . Averages and standard deviations of the best-fit Δz along with averages of $\sigma_{\text{sd,all}}$ are given in Table 6. These results show uniform Δz distribution and hence no gas motion exceeding these variations and errors. The errors for each sky region range from $\pm 0.5 \times 10^{-3}$ to $\pm 2 \times 10^{-3}$, corresponding to radial velocities of 150 and 600 km s⁻¹ respectively.

Within the inner cells, CS1–CS3 show lower Δz in the best-fit value. To further search for possible spatial variation in redshifts, we use data differently from the above case. Here we fit all spectra for each cell simultaneously with a common redshift, assuming no instrumental and systematic variation in the energy scale. We remove one observation (sequence 800010010) to avoid systematic error as mentioned above. We sorted the result as a function of the position angle of the cell with respect to the cluster center, as shown in Fig. 8. The obtained redshift are basically consistent with the above result in Fig. 7., although the given error declines because these include only statistical errors. From the inner cells (left panel Fig. 8) we found lower redshifts in easterly and westerly directions and higher redshifts toward the south. From the larger cells (left panel Fig. 8) we found some variations but more random and comparable to the possible systematic error (section 3.4; $\sim 10^{-3}$ in redshift or 300 km s⁻¹). We cannot find all variations if we use the data in summer or winter obser-

vations separately (See Fig. 7). Based on these careful analyses, we suggest a hint of lower redshift regions at $2 - 4'$ (45–90 kpc; CS1–CS3) west of the cluster center. Other variations are insignificant and possibly attributable to instrumental effects.

In a search for redshift variation on a finer scale, we divided the central $3' \times 3'$ region into 9 cells of sized $1' \times 1'$. We found a uniform redshift distribution within about $\pm 1 \times 10^{-3}$ in redshift.

4.3. Line Broadening and Turbulent Velocity

The observed spectra are used to constrain the turbulent Doppler broadening of the emission line. Following OTA07 and similar to our analysis stated in subsection 3.3, we model the Fe-line spectra by including an additional line width (σ_{add} ; a Gaussian width).

Here we note that the cluster-intrinsic lines are not a single Gaussian line, but integrate many lines. For example the emission around 6.7 keV includes not only a dominant He-like resonance line at 6700 eV but also intercombination lines at 6667-6682 eV and a forbidden line at 6636 eV along with other weak lines between the resonance and forbidden lines. Effective widths for this He-like triplet are about 30 eV for the temperature of 2–4 keV gas (OTA07). In addition, gas bulk motions unresolved spatially within the spectral extraction region and projected in the line of sight contribute to σ_{add} .

For each observation and region, we obtained σ_{add} and its upper limit. We found that in most cases σ_{add} was consistent with zero and that even using a non-zero σ_{add} did not change the best-fit redshift. These are averaged over different observations and presented in Fig. 9. The best-fit σ_{add} are all below 20 eV, except for that from CL15 where the statistics

Table 6. Statistics of redshift variations among 16 different sky regions. All values are in unit of redshift in 10^{-3} .

regions	$\langle \Delta z \rangle$	$\sigma_{\text{sd}}^{\text{a}}$	$\langle \text{err} \rangle^{\text{b}}$
CS0–CS15	-0.1	0.35	0.92
CL0–CL15	0.12	0.52	1.3

^aStandard deviation.

^bAverage of errors.

are significantly lower than others. Given the systematic error and intrinsic cluster line width, these σ_{add} are all consistent with no additional broadening due to turbulent motion. Statistical upper limits of σ_{add} are 20–50 eV, which equates to the upper limits for turbulent motion of 900–2200 km s⁻¹. We may add systematic uncertainty of 1250 km s⁻¹ (subsection 3.3).

5. LARGE-SCALE SPECTRA

Here we use a set of offset pointing data with offset angles of 14′ – 36′ from the cluster center (Table 3 and Fig. 1) and study the spatial redshift distribution on a large scale.

We extract a spectrum from the entire CCD field of view for each offset observation. Here we use the same Gaussian model as in subsection 4.2 to fit the FI 5.7–7.0 keV band spectra and measure the redshift distribution.

There are some sets of two observations (X and X_2) sharing a pointing direction but with different roll-angles. We found that these data provide consistent results within the set, hence in these pointing sets, spectra are fitted simultaneously with a common model. Examples fittings are shown in Fig. 10.

The obtained redshifts are shown in Fig. 11. We notice that G and SE regions show larger and smaller redshifts, respectively, compared with the average. These two regions, however, are in proximity each other and overlap in the sky regions by about half the area of the entire field of view. Therefore, these deviations are likely statistical or systematic errors, and do not originate entirely from the cluster gas redshift variation. When we combine these two regions, a redshift of 0.020 ± 0.001 consistent with other regions, is obtained, as shown in Fig. 11 (a star mark). Region A also shows a relatively large deviation alongside significant statistical errors. Including these deviated regions, the error-weighted average, standard deviation, and average statistical error are found to be 19.2×10^{-3} , 1.8×10^{-3} , and 1.2×10^{-3} , respectively.

Based on the above results, we conclude that gas redshifts are uniform within $\pm(1 - 2) \times 10^{-3}$ over the cluster core region ($R < 20 - 30'$) in a spatial scale of about 15′ (300 kpc). In other words, we found no systematic velocity structure exceeding $\pm(300 - 600)$ km s⁻¹.

The average and standard deviation of redshifts in the central region given in subsection 4.2) are 18.4×10^{-3} and 0.6×10^{-3} , respectively. The redshift averaged over the offset regions is consistent with that of the central region within these variations and errors.

To constrain line broadening and turbulent velocity, we performed a similar spectral

fitting as in subsection 4.3. However, lower statistics mean the limits obtained are typically weaker than those in the central regions above. We found the obtained σ_{add} to be consistent with zero turbulent velocity and statistical upper limits of σ_{add} of 20–70 eV, corresponding to velocities of 900–3000 km s⁻¹.

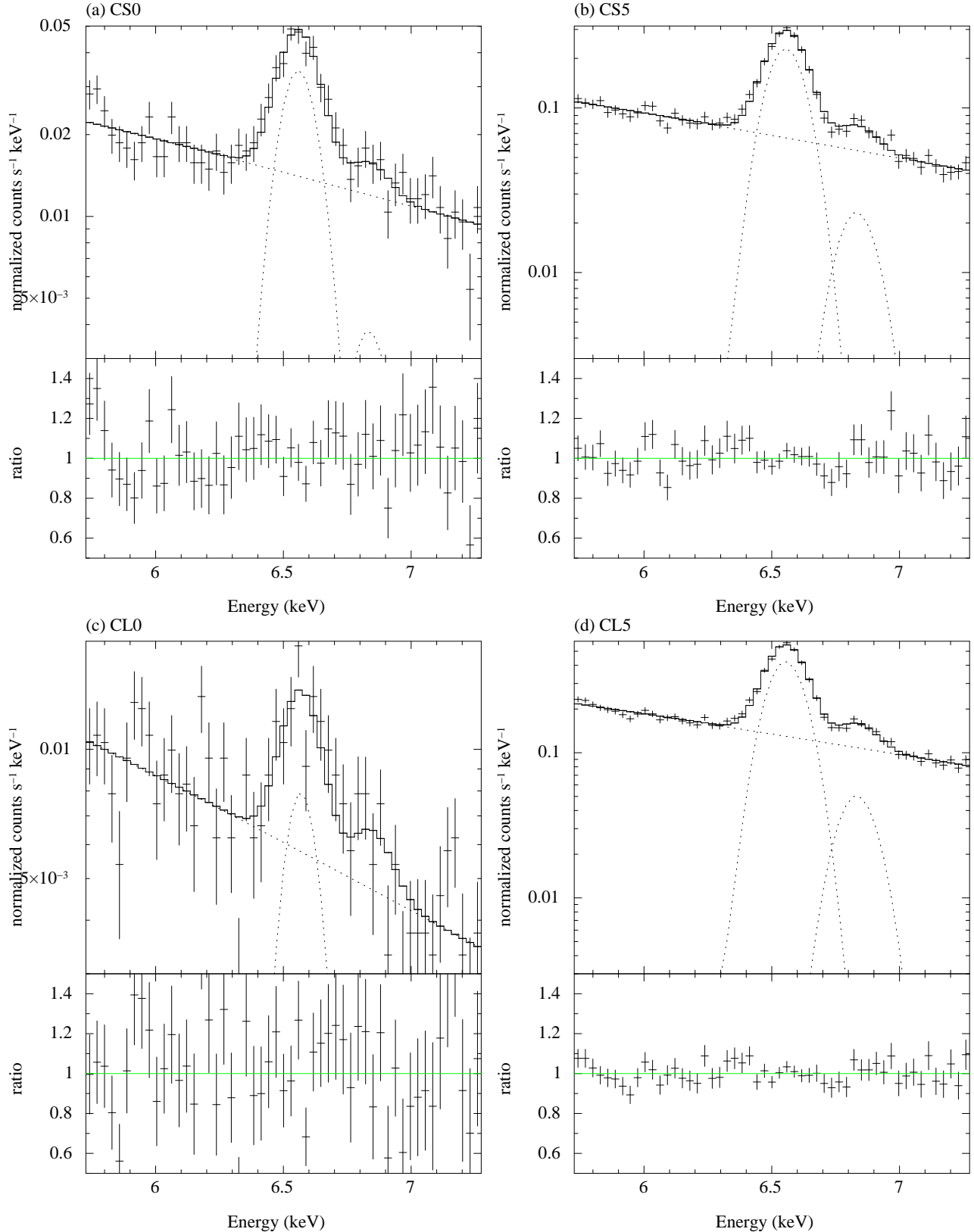


Fig. 5.— Example of the redshift determination. The spectral fit from one sequence (104018010) of cells CS0, CS5, CL0, and CL5 is shown from the top left to the bottom right. In the upper panels of each plot, the data, best-fit model, and model components are shown by crosses, solid-histogram, and dotted lines, respectively. In the lower panels fit

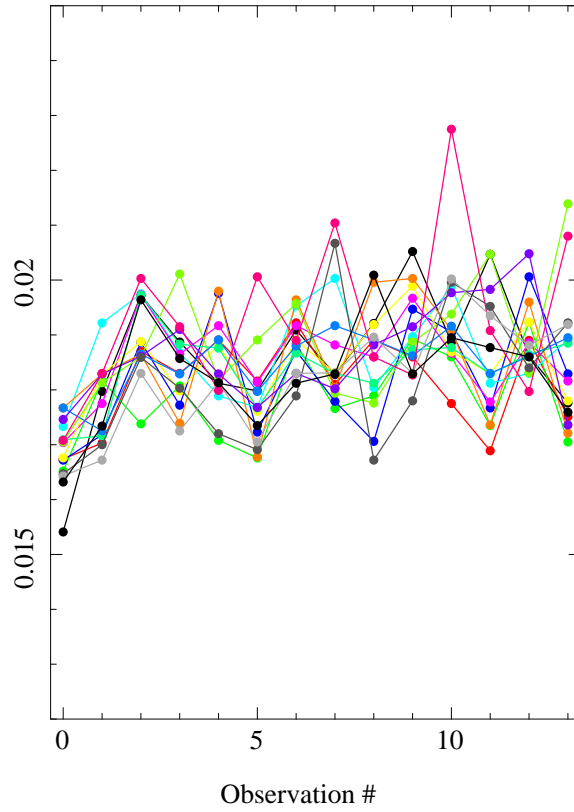


Fig. 6.— Obtained redshifts as a function of observation time (sequences) for different sky regions (CS0 to CS15). Statistical errors are about $\pm 0.5 \times 10^{-3}$ and $\pm 0.8 \times 10^{-3}$ on average for inner and outer cells, respectively.

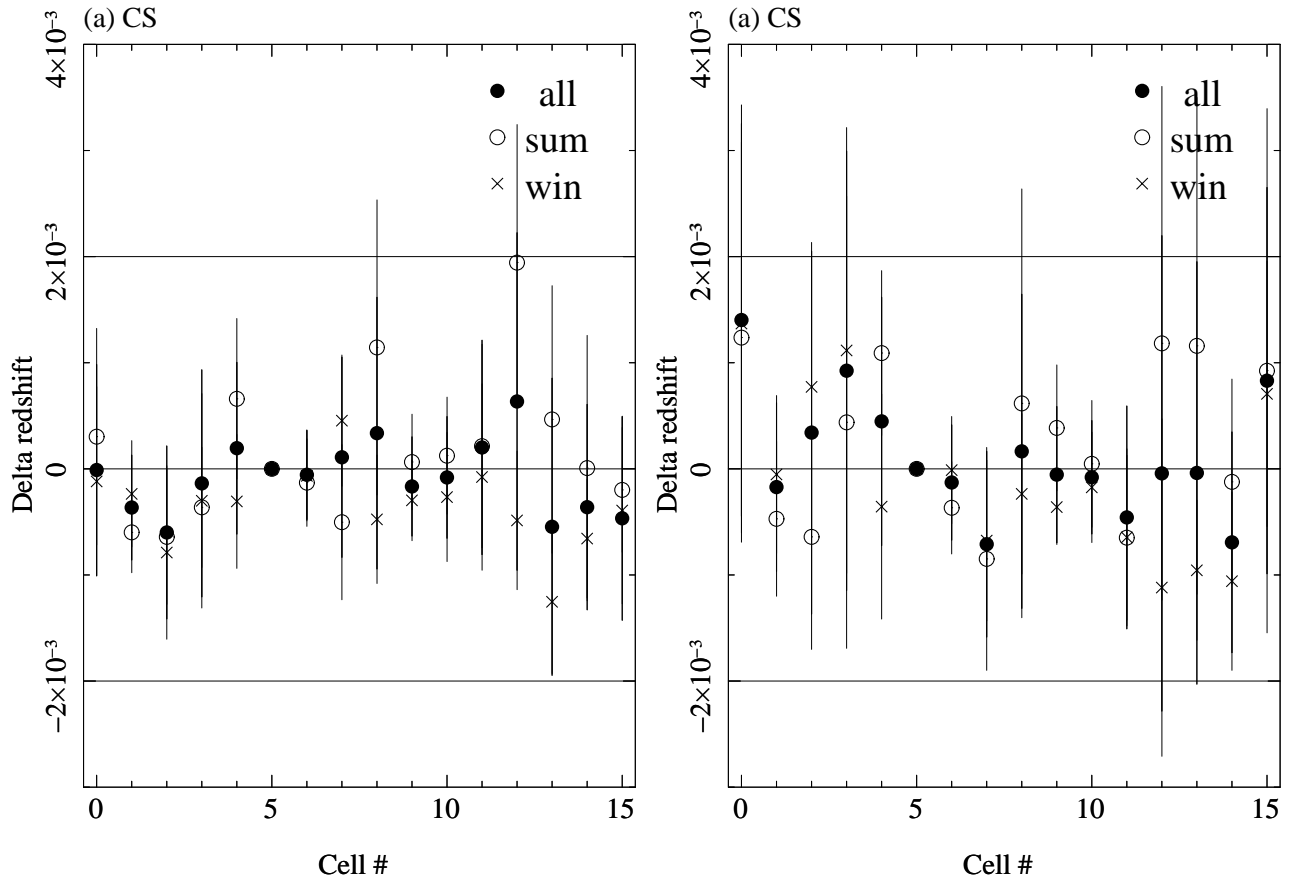


Fig. 7.— Obtained redshifts as a function of sky regions. Left and right panels show results of inner cells (CS0 to CS15) and outer cells (CL0 to CL15), respectively. Error bars are shown only for all observations.

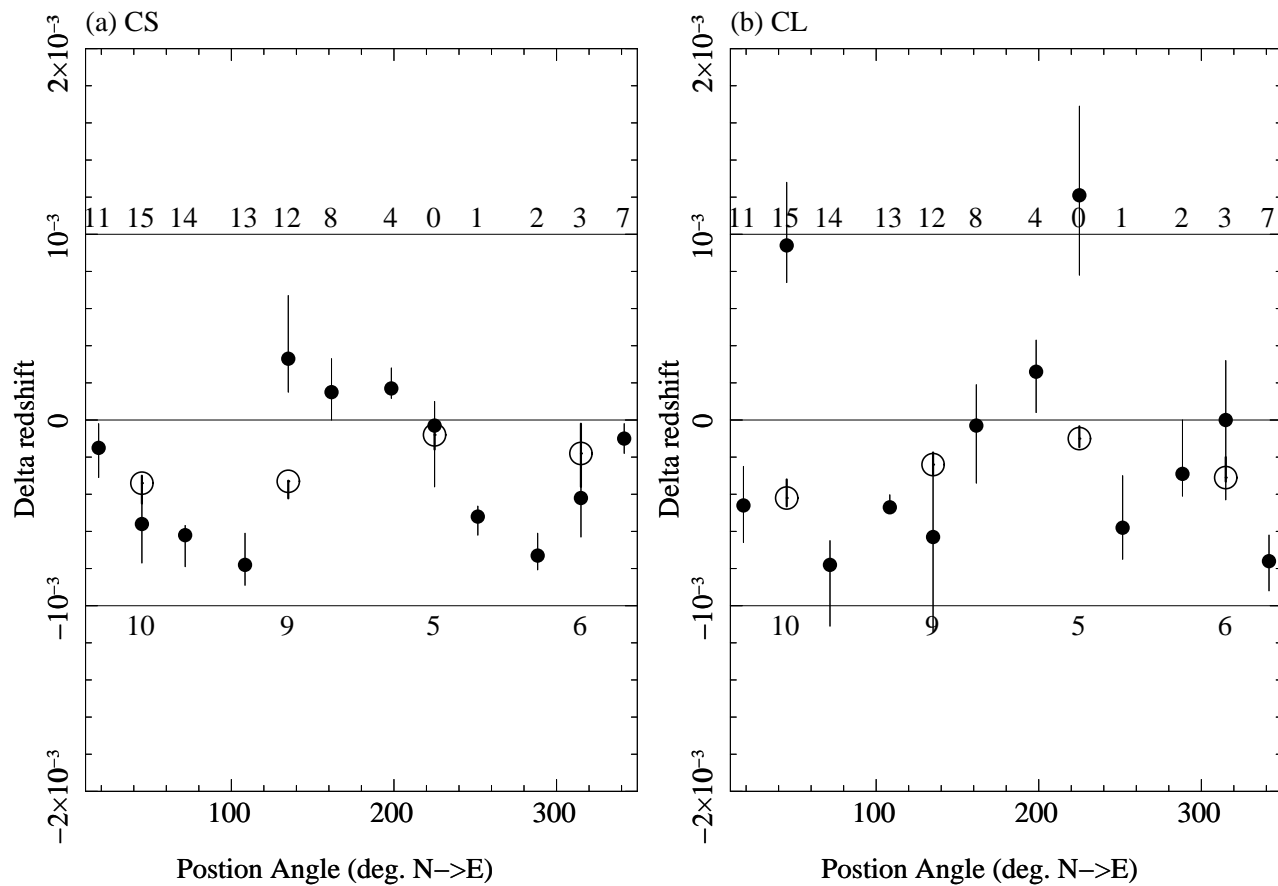


Fig. 8.— Obtained redshifts as a function of position angle (north to east). Panels (a) and (b) show results of smaller cells (CS0–CS15) and from larger cells (CL0–CL15), respectively. Filled- and open-circles are from the outer twelve cells and inner four cells, respectively, for each region. Numbers in panels indicate cell numbers.

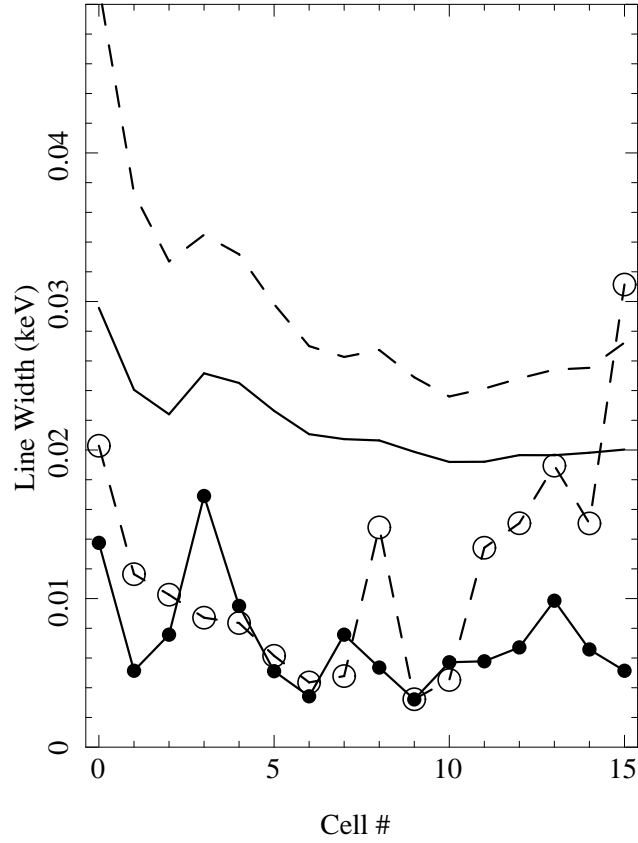


Fig. 9.— Additional line widths, σ_{add} (circle marks), and their upper limits (line) from different sky regions, averaged over different observations. Results from smaller cells and larger cells are shown by solid and dashed-lines, respectively. Note that at CL15 σ_{add} exceeds its upper limit, because both are average values from different observations.

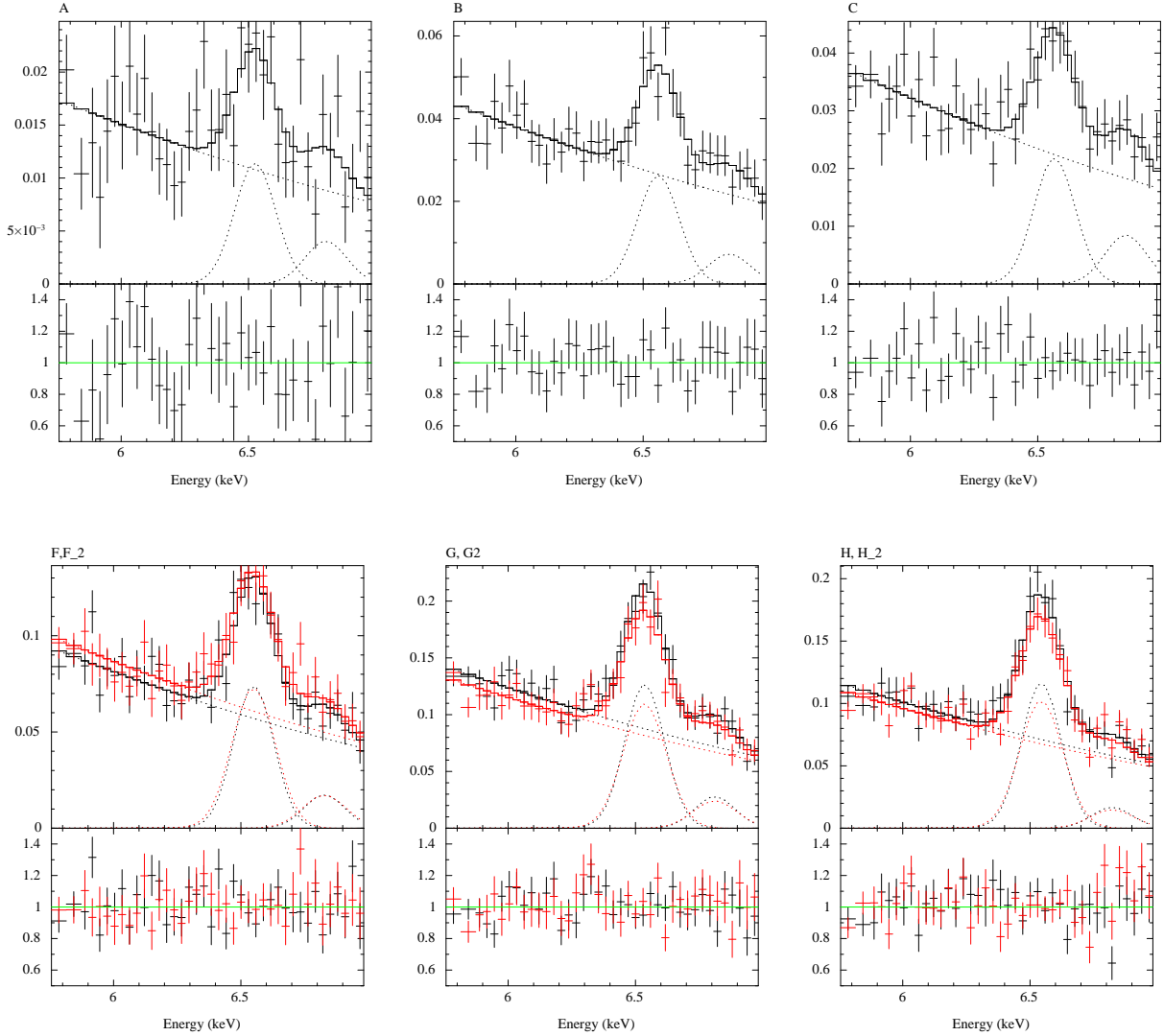


Fig. 10.— Example of spectral fitting from offset pointing data, which are used to measure redshifts. From top left to bottom right, the spectra from regions A, B, C, F, G, and H are shown. For each plot, in the upper panels the data, best-fit model, and model components in counting units of $s^{-1} \text{keV}^{-1}$ are shown. In the lower panels fit residuals in terms of the data to model ratio are shown.

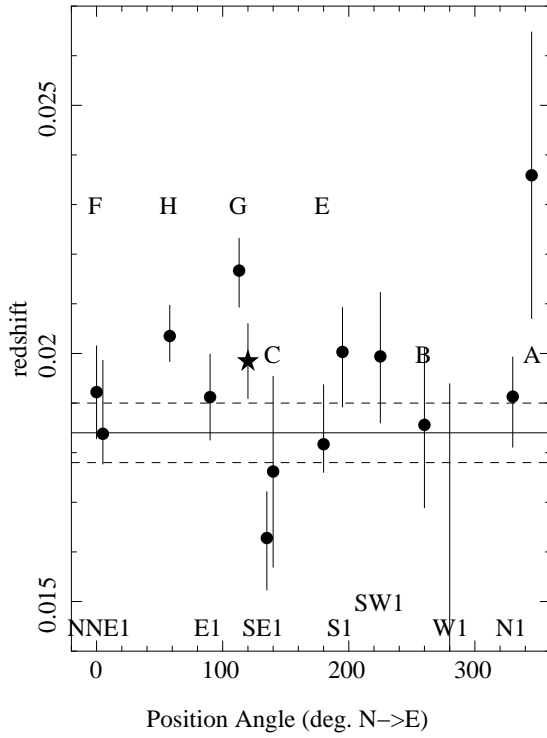


Fig. 11.— Redshift distribution from offset observations as a function of position angles of the pointing. The star mark shows the redshift obtained by a simultaneous fit of G and SE regions. The horizontal solid and dashed lines indicate the average and standard variation from the central pointing (subsection 4.2).

6. SUMMARY AND DISCUSSION

6.1. Spatial Mixing

The photon mixing caused by the *Suzaku* telescopes and projection effects meant the measured velocity variation was diluted compared with the intrinsic three dimensional variation.

The point spread function of the telescopes include half-power diameters of $1'.8 - 2'.3$ and 90% fraction encircled-energy radii of $2'.5 - 3'.0$, meaning variations below these scales would be smoothed. It is also difficult to separate the gas velocity of a faint emission component. This effect was examined by a ray-tracing simulation in OTA07 for the *Suzaku* measurements in the Centaurus cluster. They found that when $2' \times 2'$ cells are used at the core, about 50-60% of the events collected by each cell originate from the surrounding eight cells. Because the Perseus cluster has a central surface brightness distribution similar to that of Centaurus, our measurement in the central region with $2'.2$ width cells (CS0 to CS15) is similarly affected. For the outer cells with a $4'.4$ width (CL0 to CL15), mixing effects should be much smaller ($< 10\%$).

In the large-scale measurements (section 5), photon mixing due to stray X-rays from the bright center could be an additional contamination. We estimate, however, that photons scattered from the central region to offset regions with a typical offset angle of $15 - 20'$ represent a minute percentage of all photons within each offset pointing and we could hence ignore this mixing.

6.2. Summary of Results and Comparison with Previous Studies

Dupke & Bregman (2001) claimed a radial velocity difference in the Perseus cluster using the ASCA GIS. They compared spectra collected at the center and offsets separated by more than $40'$. These spatial scales exceed our study within radii of $30'$, which means these two measurements cannot be compared.

We summarize the limits we determined for gas motion along with related parameters in Table 7. For comparison, results of OTA07 are also presented. Both results of the *Suzaku* XIS are limited by similar levels of systematic errors from the energy scale calibration. The levels of statistical errors between the two are also comparable.

As described in section 1, gas velocity measurements are important to calibrate the hydrostatic equilibrium (H.E.) mass estimation. OTA07 converted velocity variation obtained

into rotational motion and approximated the uncertainty of the H.E. mass by gas kinetic to thermal energy ratio. The ratio is proportional to $fM^2 = f(\frac{v}{c_s})^2$, where f , v and M are the fraction, velocity, and Mach number of the moving gas and c_s is the gas sound velocity (given in Table 7). The uncertainty of the rotation angle introduces another error.

Our limits on gas bulk velocities and hence on M are comparable to those in OTA07. The wider physical size covered by our observations (row R in Table 7) allowed us to constrain the gas motion and hence the total mass within a volume significantly exceeding that in OTA07. This is an important step to measure total masses in cluster scales. Provided the Fe-K line emission of the Perseus central region is exclusively brighter than other nearby clusters, this system could represent a unique measurement of the gas motion at the cluster scale via current CCD-type instruments. The decreasing X-ray surface brightness hinders efforts to constrain the motion beyond our achieved scale. It will also remain challenging to reach out beyond cluster core regions even with near-future high energy resolution instruments such as SXS (Mitsuda et al. 2010) onboard ASTRO-H (Takahashi et al. 2010) without a large collecting area.

6.3. Dynamics in the Core

In and around NGC 1275, complex interactions occur among various gaseous components, high-energy particles from the AGN and radiation from stars and AGN, and probably magnetic fields. Nearby galaxies as well as the central galaxy may have moved around within the growing gravitational potential. In this active environment, the ICM should have various types of motions. Observationally, the lack of resonant scattering of the Fe-K line at the Perseus core indicates gas motions of $M > 0.5$ (Churazov et al. 2004). It is crucial to measure the energies in these gas motions in our study.

We found a hint of gas bulk motions within the cluster core (Fig. 8; $R < 4'.4$), while the key detection was lower velocities in regions 2 – 4' west of center. West of center, clear X-ray enhancement was found as seen in Fig. 4. Churazov et al. (2003) interpreted this structure as a result of a past minor merger in an east-west direction. The obtained gas motion is consistent with this minor merger model and additionally suggests a velocity component in the line of sight. Because we observe a mix of photons from the sub component and main cluster due to the sky projection and the telescope point spread function, the real gas velocity of the sub exceeds the observed figure ($v_{\text{obs}} = 150 - 300 \text{ km s}^{-1}$). If we assume f to be the emission fraction from the sub, v_{obs} can be approximated with sub and main velocities (v_{sub} and v_{main}) as $v_{\text{obs}} = fv_{\text{sub}} + (1 - f)v_{\text{main}}$. In this case, the relative velocity with respect to v_{main} can be estimated as $\Delta v_{\text{sub}} \sim f^{-1}\Delta v_{\text{obs}}$. From the relative deviation map of the surface

Table 7. Summary of gas velocity limits.

		Perseus (center)	Perseus (large)	Centaurus
	(unit)	section 4	section 5	OTA07
redshift		0.0183	–	0.0104
1'	(kpc)	22.2	–	15.3
kT ^a	(keV)	4.5	6	3
c_s ^b	(km s ⁻¹)	1100	1300	900
region size ^c		2'.2/4.4'	18'	2'.1
	(kpc)	50/100	400	30
R ^d	(kpc)	200	600	150
Δv_{bulk} ^e	(km s ⁻¹)	300–400	550	700
		± 300 (sys.)	± 300 (sys.)	± 500 (sys.)
v_{turb} ^f	(km s ⁻¹)	900–2200	900–3000	900
	(km s ⁻¹)	± 1250 (sys.)	± 1250 (sys.)	± 1250 (sys.)

^aTypical ICM temperature within the measured region. The Perseus temperatures are taken from spectroscopic result in Tamura et al. (2009), while that of the Centaurus from OTA07.

^bSound speed at the ICM temperature.

^cIndividual region sizes.

^dAveraged separation among regions.

^eUpper limit of the velocity variation. Systematic error is indicated by 'sys'. Limits are taken from the standard deviation from samples.

^fUpper limit of the turbulent velocity.

brightness (Fig. 4), we estimate f to be 0.2–0.4. In this case, Δv_{sub} could be 500–1000 km s⁻¹. Interestingly, the second optically-bright member galaxy, NGC 1272, sitting on a rim of the west sub structure ($\sim 5'$ WWS of NGC 1275), also has a lower radial velocity than that of NGC 1275 by ~ 1100 km s⁻¹. Furthermore, the chain of galaxies further west has an average radial velocity lower than the cluster center by about 1500 km s⁻¹. We suggest the association of the obtained gas velocity structure with these galaxies. We discuss these gas and galaxy relations on a larger scale in the next subsection.

Using the obtained measurements, we estimate kinetic energy (E_{kin}) by gas bulk motion. As stated in section 6.2, E_{kin} relative to the thermal energy (E_{th}) in the gas can be presented by $fM_{\text{bulk}}^2 = f(\frac{\Delta v_{\text{bulk}}}{c_s})^2$. Using the relation between $\Delta v_{\text{sub}} \rightarrow \Delta v_{\text{bulk}}$ and Δv_{obs} given above, $E_{\text{kin}}/E_{\text{th}}$ becomes $f^{-1}(\frac{v_{\text{obs}}}{c_s})^2$. Assuming c_s of 1100 km s⁻¹ and f of 0.2 – 0.4, the observed Δv_{obs} (150–300 km s⁻¹) gives $E_{\text{kin}}/E_{\text{th}} = 0.1 – 0.3$. Fabian et al. (2011) estimated the energy associated with non-radial structure (E_{d}) based on variation in the gas pressure map. This energy should be closely related to E_{kin} estimated here. They estimated $E_{\text{d}}/E_{\text{th}}$ to be within a few percent at radii of ~ 110 kpc corresponding to the west sub component region. Because both estimations are order of magnitude, we cannot compare these quantitatively. These estimations are among the first attempts to measure all the energy components in the cluster gas and understand the energy distribution of clusters.

The west system is the largest substructure within the core. Our measurement also indicates that it has the largest bulk velocity, at least in a radial direction, which means this structure could have the largest kinetic energy due to bulk motion. We found no other systematic motions around the core with scales > 20 kpc and bulk velocities exceeding half the sound velocity (~ 550 km s⁻¹). This is consistent with the observation that any other features revealed around the core are below 10 kpc (30'') in size. These structures are also likely to have velocities not exceeding the virial velocity of the central galaxy, or about 200 km s⁻¹. The lack of heated gas or strong shock (Fabian et al. 2003) also pointed to no sonic or super sonic motion. We conclude that within much of the cluster core volume, the gas remains in hydrostatic equilibrium.

In Table 8 we present radial velocities of NGC 1275 and the cluster from optical data and this X-ray results. The optical radial velocity of NGC 1275 differs from that of a mean of cluster member by only about 200 km s⁻¹, demonstrating that the galaxy remains at the bottom of the cluster potential. The absolute radial velocity of the gas at the core is consistent with that of the galaxy in optical within the errors from X-ray data. This indicates that large parts of stars and the gas in and around the galaxy stay together at the bottom of the cluster potential center. The cluster gas on a large scale also has a mean velocity consistent with that in optical, confirming that these two baryonic components

beyond galaxy scale remain together at the same potential center. These comparisons in absolute redshifts are among the first attempts involving clusters.

Gas dynamics in cluster cool cores has been studied by numerical simulations. For example, Ascasibar & Markevitch (2006) simulated off-axis minor mergers and gas sloshing and reproduce cold fronts. They presented evolutions of gas velocity structures. Compared with large velocity variations in their representative runs, our measured variations (Figs. 3 and 8) are more uniform spatially and close to their results for late stages (e.g. 6/4.8 Gyr in Fig.5/10 of Ascasibar & Markevitch 2006). Note that our Doppler measurements are not sensitive to motions in the plane of the sky and diluted by projection. In fact in the Perseus cluster gas spiral flows in the plane of the sky are suggested from X-ray images (e.g. Fabian et al. 2011; Simionescu et al. 2012). Focusing on AGN jet-driven bubbles, Heinz et al. (2010) simulated high-resolution X-ray spectroscopy of nearby clusters including the Perseus cluster. They found the velocity structure of the bubbles in this core with energy shifts of about 350 km s^{-1} , which are close to our limit. However, these structures are too small in size ($< 10 \text{ arcsec}$) and too faint in X-ray brightness contrast to resolve by the current data.

6.4. Large-Scale Dynamics

We found an absence of gas bulk motion on a large scale. Our upper limit for the radial gas velocity is about 600 km s^{-1} , which implies either that gas motion in the cluster is predominantly in the plane of the sky or subsonic at most.

In subsection 6.3 we discussed the potential of the gas motion around the western core being associated with galaxy motions. The associated chain of galaxies is further distributed toward west. To study the gas and galaxies relation in the west and larger areas, we compare our derived gas dynamics with that in galaxies in the cluster.

We use the following two catalogs as the deepest collections of galaxies in the Perseus cluster. The CfA redshift catalog (Huchra et al. 1995) includes 94 (120) galaxies with radial velocities within $30'$ ($60'$) of the cluster center, while the 2MASS redshift survey (Huchra et al. 2012) includes 66 (103) galaxies in the same regions but with complete photometric data. Fig. 12 shows the radial velocities of galaxies within a radius of $30'$ of the center as a function of azimuthal angles relative to the center. Most galaxies are distributed around the cluster dynamical center at redshift of ~ 0.018 , corresponding to that of NGC 1275. This is consistent with early studies of galaxy distributions (e.g Kent & Sargent 1983). Some galaxies have higher or lower velocities ($\Delta v > 2000 \text{ km s}^{-1}$), which may be contamination

dynamically unrelated to the main system.

We include gas velocities from Fig. 11 into Fig.12, which is the first such comparison. In galaxy velocities, there are some local structures, the clearest of which is a group at an angle of around 260° with lower velocities ($-2000 \text{ km s}^{-1} < \Delta v < 1000 \text{ km s}^{-1}$). This is part of the chain of galaxies mentioned in subsection 6.3, which should be before or after a collision into the main cluster centered on NGC 1275. Based on the X-ray distribution around the core, Churazov et al. (2003) suggested that the substructure is after a collision about 0.25 Gyr ago. Based on comparison between the galaxy and gas velocities around this angle at the cluster west, we notice that the gas is closer to the cluster center than galaxies at this azimuth. Note that these galaxies in total exceed the cD galaxy in terms of luminosity and hence mass. If these two baryonic components are associated, what explains this difference? We note a difference in effective radii between the two wavelength bands. The X-ray emission is weighted toward the inner region, due not only to the positions of spectral extractions (Fig. 1) but also the density-squared X-ray emission intensity. Considering these effects, the effective radius of the X-ray data can be approximated around $10'$. On the other hand, galaxies in the west are uniformly distributed over the $30'$ radius region. These galaxies are point sources in X-ray without any bright extended excess emission (Fabian et al. 2011). In addition, this difference suggests a segregation between the two components during a violent collision. Such detachments in the sky position have been observed in some merging systems such as the Bullet (Clowe et al. 2006). Our measurement is a new approach to reveal such actions not only in spatial terms but also in the radial velocity space. Note that in the major-merger system Abell 2256 Tamura et al. (2011) revealed that gas and galaxies move in pairs within radial velocity and spatial spaces.

Based on ASCA observations Furusho et al. (2001) observed an extended cool region $10-20'$ east of the cluster center, alongside a ring-like region surrounding the east cool region and the core. They suggested a past collision of a poor cluster in a direction nearly parallel to the line of sight. Our observation covers a substantial fraction of the east cool region as shown in Fig. 1. To limit the current velocity of the east sub system we must assume the X-ray emission fraction of the moving system within the extracted spectra. We estimate this at 0.3–0.5 according to the relative deviation map of surface brightness in Churazov et al. (2003). Combining this with our measurement in Fig. 11 ($\Delta v < 600 \text{ km s}^{-1}$), we constrain the radial velocity of the sub system $< (1200 - 2000) \text{ km s}^{-1}$.

In future we would cover more galaxies by conducting deeper surveys and deep X-ray spectra covering larger volumes in a number of systems. Gravitational lensing would also measure dark matter distributions. Direct comparisons between these three components in dynamical and spatial distributions should reveal a number of local events and measure the

dynamical cluster age, thus giving a systematic picture of structure formation of gas and galaxies but invisibly controlled by dark matter.

Considering that the virial radius (r_{vir}) of the cluster is 2.2 Mpc (or $\simeq 100'$), we measured the gas motion typically around $R \simeq 0.1 - 0.3r_{\text{vir}}$. The obtained upper limits for the bulk motions are typically $(\Delta v_{\text{bulk}}/c_s) \lesssim 0.5$ taking account of the systematic errors. The turbulent motions are more loosely constrained ($v_{\text{turb}} \gtrsim c_s$). Cosmological cluster simulation results suggest that the kinematic energy of the gas is expected to be left only in the level of $\sim 10\%$ of the thermal energy in the corresponding radius range (e.g. Lau et al. 2009; Vazza et al. 2009). Furthermore, this value tends to be even lower for a sub sample of relaxed clusters. Therefore, our results of the absence of both the bulk and turbulent motions except for the some hints at west of the core are consistent with these simulations.

6.5. Turbulent Motion

In addition to the gas bulk motion, we searched for the turbulent motion using the line width. We obtained the limits generally larger than the sound speed as given in Table 7. OTA07 also reported a limit of the turbulence using the XIS data of the Centaurus integrated over a large region of $18' \times 18'$ (Table 7). These two limits are similar to each other, because that both limits depend largely on the energy resolution of the XIS and its calibration. Our result is the first attempt to constrain the turbulent motion based on the spatially-resolved line X-ray spectra.

The gas turbulent (random) motion could introduce an error on the H.E. mass estimate. The additional mass or kinetic energy due to the turbulence can be approximated by the factor given in subsection 6.3, M^2 with the turbulent velocity, v_{turb} replaced as v . We obtained the limit on v_{turb} a few times larger than that on the bulk velocity (Table 7). Therefore the uncertainty from the turbulent motion dominates that from the ordered one.

The *XMM-Newton* RGS was used to constrain the gas turbulent motions in hot gas in clusters and galaxies (e.g. Xu et al. 2002). Sanders & Fabian (2013) analyzed RGS spectra of dozens of sources and found evidence for $> 400 \text{ km s}^{-1}$ velocity line broadening and limits down to 300 km s^{-1} for some systems. The RGS spectra can be used only for centrally-peaked X-ray line emission below 1.5 keV (dominated by Fe-L lines) and results are coupled with the brightness distribution of the line emission which is not straightforward to model.

As described in subsection 4.3, the limit on v_{turb} is mostly limited by the instrumental energy resolution. Therefore to improve the limit significantly high energy resolution instruments such as X-ray calorimeters are necessary. For example, direct and robust study

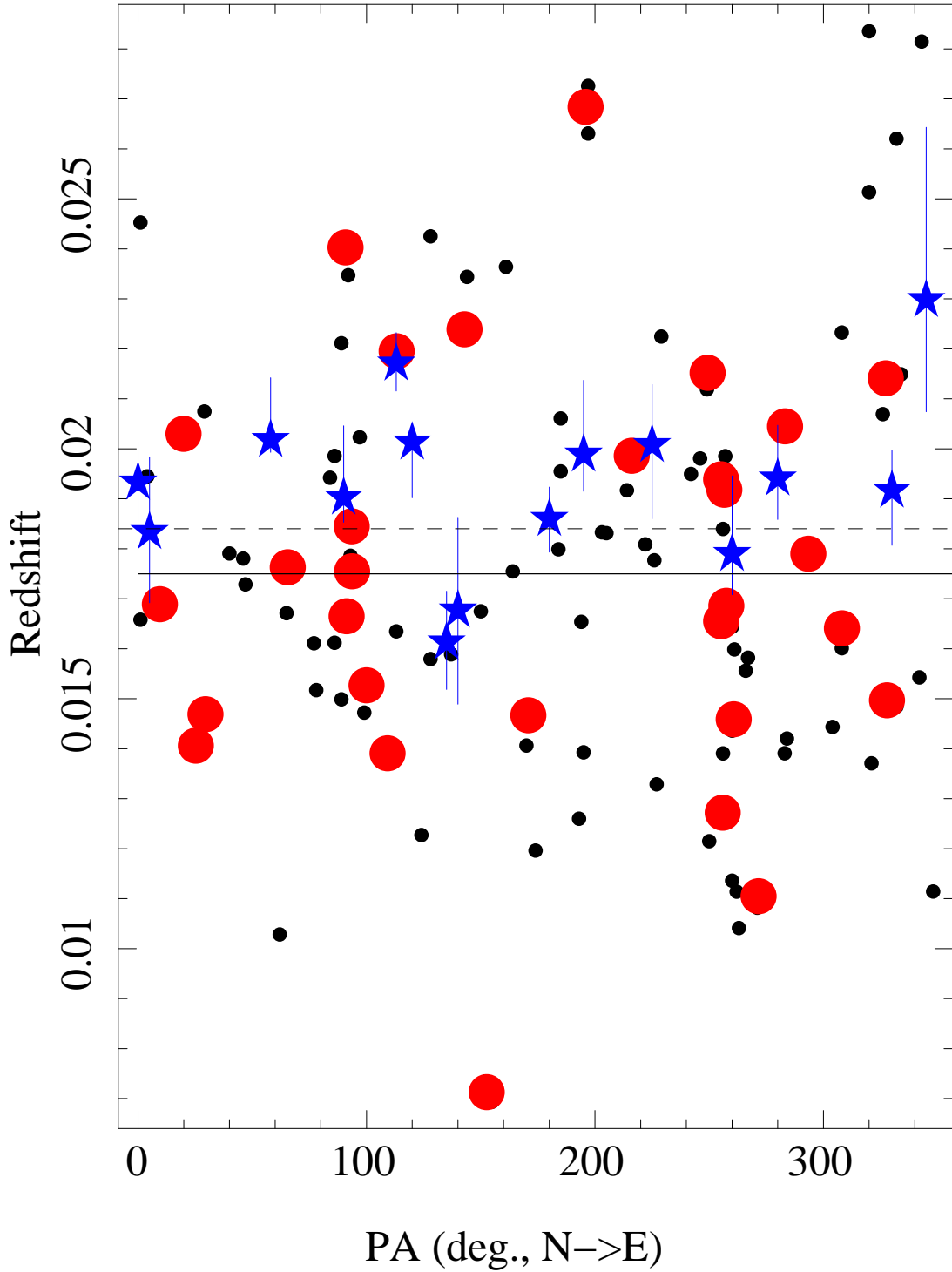


Fig. 12.— Radial velocity distributions of galaxies and gas as a function of the position angle. The small (black) and large (red) circles indicate galaxies from the CfA redshift catalog (94 galaxies) and bright galaxies (K-band magnitude < 10.7) from the 2MASS redshift catalog. There are some overlaps between the two samples. The velocity of NGC 1275 is shown by a solid line. Star marks indicate the gas velocity taken from Fig. 11. The central velocity of the gas components is shown by a dashed line.

will be obtained by SXS onboard ASTRO-H , providing 5–7 eV (FWHM) energy resolution, corresponding to 300 km s^{-1} at the Fe-K line. A 100 ksec SXS observation of the Perseus center provides more than 10,000 counts in the He-like triplet emission and measurements of the turbulent along with those of bulk velocity structure.

We thank the referee for useful comments and suggestions. *Chandra* image of the Perseus cluster was provided kindly by J.Sanders. We thank all the *Suzaku* team member for their supports. We acknowledge the support by a Grant-in-Aid for Scientific Research from the MEXT, No.24540243 (TT), No.25400231 (NO), and No.A2411900 (SU).

REFERENCES

- Arnaud, K. A. 1996, *Astronomical Data Analysis Software and Systems V*, 101, 17
- Ascasibar, Y., & Markevitch, M. 2006, *ApJ*, 650, 102
- Böhringer, H., Voges, W., Fabian, A. C., Edge, A. C., & Neumann, D. M. 1993, *MNRAS*, 264, L25
- Clowe, D., Bradač, M., Gonzalez, A. H., Markevitch, M., Randall, S. W., Jones, C., & Zaritsky, D. 2006, *ApJ*, 648, L109
- Churazov, E., Forman, W., Jones, C., Böhringer, H. 2003, *ApJ*, 590, 225
- Churazov, E., Forman, W., Jones, C., Sunyaev, R., Böhringer, H. 2004, *MNRAS*, 347, 29
- Dupke, R. A., & Bregman, J. N. 2001a, *ApJ*, 547, 705
- Evrard, A. E., Metzler, C. A., & Navarro, J. F. 1996, *ApJ*, 469, 494
- Fabian, A. C., Sanders, J. S., Allen, S. W., et al. 2003, *MNRAS*, 344, L43
- Fabian, A. C., Johnstone, R. M., Sanders, J. S., et al. 2008, *Nature*, 454, 968
- Fabian, A. C., Sanders, J. S., Allen, S. W., et al. 2011, *MNRAS*, 418, 2154
- Fujita, Y., et al. 2008, *PASJ*, 60, 1133
- Furusho, T., Yamasaki, N. Y., Ohashi, T., Shibata, R., & Ezawa, H. 2001, *ApJ*, 561, L165
- Hayato, A., Yamaguchi, H., Tamagawa, T., et al. 2010, *ApJ*, 725, 894

- Heinz, S., Brügggen, M., & Morsony, B. 2010, *ApJ*, 708, 462
- Huchra, J. P., Geller, M. J., Clemens, C. M., Tokarz, . P., Michel, A. 1995, The CfA Redshift Catalogue, Version June 1995, Harvard-Smithsonian Center for Astrophysics [<http://vizier.cfa.harvard.edu/viz-bin/Cat?VII/193>]
- Huchra, J. P., Macri, L. M., Masters, K. L., et al. 2012, *ApJS*, 199, 26
- Hirayama, Y., & Ikeuchi, S. 1978, *Progress of Theoretical Physics*, 60, 1337
- Kent, S. M., & Sargent, W. L. W. 1983, *AJ*, 88, 697
- Koyama, K, et al. 2007, *PASJ*, 59, S23
- Lau, E. T., Kravtsov, A. V., & Nagai, D. 2009, *ApJ*, 705, 1129
- Markevitch, M., & Vikhlinin, A. 2007, *Phys. Rep.*, 443, 1
- Matsushita, K., Sakuma, E., Sasaki, T., Sato, K., & Simionescu, A. 2013, *ApJ*, 764, 147
- Mitsuda, K, et al. 2007, *PASJ*, 59, S1
- Mitsuda, K., et al. 2010, *Proc. SPIE*, 7732,
- Nagai, D., Vikhlinin, A., & Kravtsov, A. V. 2007, *ApJ*, 655, 98
- Werner, N., Urban, O., Simionescu, A., & Allen, S. W. 2013, *Nature*, 502, 656
- Nishino, S., Fukazawa, Y., Hayashi, K., Nakazawa, K., & Tanaka, T. 2010, *PASJ*, 62, 9
- Nishino, S., Fukazawa, Y., Hayashi, K. 2012, *PASJ*, 64, 16
- Ota, N., et al. 2007, *PASJ*, 59, 351 (OTA07)
- Ozawa, M., et al. 2009, *PASJ*, 61, 1
- Sanders, J. S., & Fabian, A. C. 2013, *MNRAS*, 429, 2727
- Sato, K., Matsushita, K., Ishisaki, Y., et al. 2008, *PASJ*, 60, 333
- Sato, T., Matsushita, K., Ota, N., et al. 2011, *PASJ*, 63, 991
- Sawada, M., Nakashima, S., Nobukawa, M., Uchiyama, H., & XIS Team 2012, *American Institute of Physics Conference Series*, 1427, 245
- Serlemitsos, P. et al. 2007, *PASJ*, 59, S9

- Simionescu, A., Allen, S. W., Mantz, A., et al. 2011, *Science*, 331, 1576
- Simionescu, A., Werner, N., Urban, O., et al. 2012, *ApJ*, 757, 182
- Sugawara, C., Takizawa, M., & Nakazawa, K. 2009, *PASJ*, 61, 1293
- Suto, D., Kawahara, H., Kitayama, T., et al. 2013, *ApJ*, 767, 79
- Takahashi, T., et al. 2010, *Proc. SPIE*, 7732,
- Takizawa, M., Nagino, R., & Matsushita, K. 2010, *PASJ*, 62, 951
- Tamura, T., et al. 2009, *ApJ*, 705, L62 (T09)
- Tamura, T., Hayashida, K., Ueda, S., & Nagai, M. 2011, *PASJ*, 63, 1009
- Uchiyama, H. et al. 2009, *PASJ*, 61, S9
- Vazza, F., Brunetti, G., Kritsuk, A., et al. 2009, *A&A*, 504, 33
- Xu, H., Kahn, S. M., Peterson, J. R., et al. 2002, *ApJ*, 579, 600

A. Energy scale calibrations

Fig. 13.— Example of the fitting of spectra sorted by detector coordinates. The axis units are the same as those in previous spectral plots. These are used in section 3.

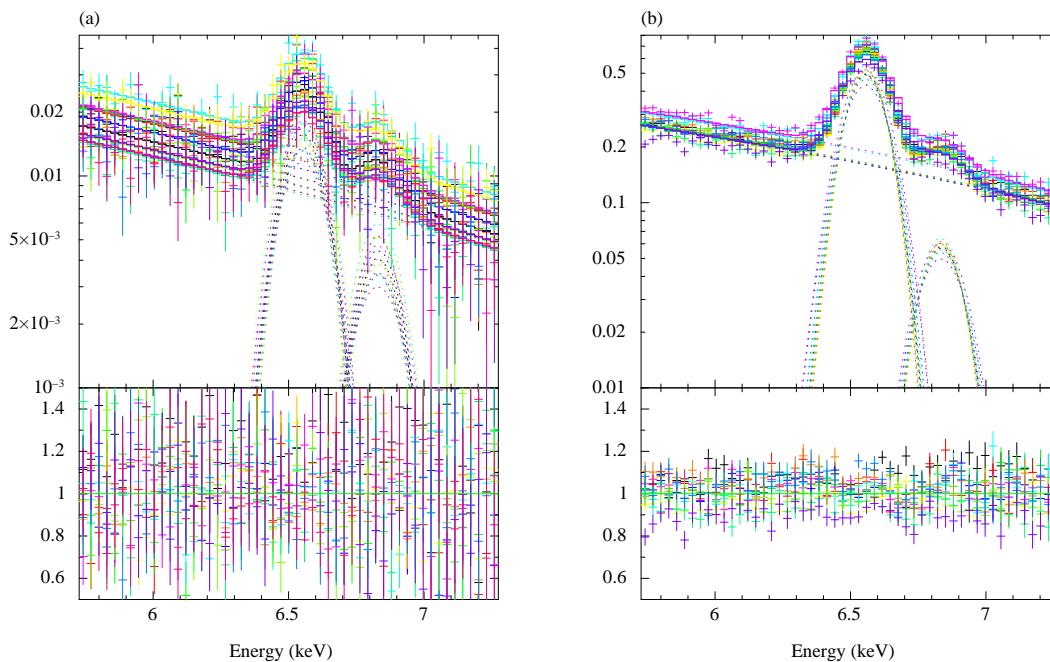


Table 8. Radial velocities of galaxies and X-ray gas.

target	velocity (km s^{-1})	error (km s^{-1})	Reference
NGC 1275	5250	20	1
member galaxy mean	5470	100	2
X-ray gas at center	5520	300	section 4 and 5
X-ray gas at $R < 15'$	5760	600	section 5

References. — (1) NED database; (2) Kent & Sargent (1983).